ECS Journal of Solid State
Science and Technology

Band Alignment of Al_2O_3 on α-$(Al_xGa_{1-x})_2O_3$

To cite this article: Xinyi Xia *et al* 2022 *ECS J. Solid State Sci. Technol.* **11** 025006

ECS Journal of Solid State Science and Technology, 2022 **11** 025006
2162-8777/2022/11(2)/025006/8/$40.00 © 2022 The Electrochemical Society ("ECS"). Published on behalf of ECS by IOP Publishing Limited

Band Alignment of Al_2O_3 on α-$(Al_xGa_{1-x})_2O_3$

Xinyi Xia,[1,*] Nahid Sultan Al-Mamun,[2] Chaker Fares,[1] Aman Haque,[2] Fan Ren,[1,] Anna Hassa,[3] Holger von Wenckstern,[3] Marius Grundmann,[3] and S. J. Pearton[4,**,z]**

[1]*Department of Chemical Engineering, University of Florida, Gainesville, Florida 32611, United States of America*
[2]*Department of Mechanical Engineering, The Pennsylvania State University, University Park, Pennsylvania 16802, United States of America*
[3]*Universität Leipzig, Felix-Bloch-Institut für Festkörperphysik, 04103 Leipzig, Germany*
[4]*Department of Materials Science and Engineering, University of Florida, Gainesville, Florida 32611, United States of America*

X Ray Photoelectron Spectroscopy was used to measure valence band offsets for Al_2O_3 deposited by Atomic Layer Deposition on α-$(Al_xGa_{1-x})_2O_3$ alloys over a wide range of Al contents, x, from 0.26–0.74, corresponding to a bandgap range from 5.8–7 eV. These alloys were grown by Pulsed Laser Deposition. The band alignments were type I (nested) at x <0.5, with valence band offsets 0.13 eV for x = 0.26 and x = 0.46. At higher Al contents, the band alignment was a staggered alignment, with valence band offsets of − 0.07 eV for x = 0.58 and −0.17 for x = 0.74, ie. negative valence band offsets in both cases. The conduction band offsets are also small at these high Al contents, being only 0.07 eV at x = 0.74. The wide bandgap of the α-$(Al_xGa_{1-x})_2O_3$ alloys makes it difficult to find dielectrics with nested band alignments over the entire composition range.
 [DOI: 10.1149/2162-8777/ac546f]

Manuscript submitted December 1, 2021; revised manuscript received January 27, 2022. Published February 21, 2022. *This paper is part of the JSS Focus Issue on Advances in Energy, Electronic and Dielectric Materials Development: From Methods to Applications.*

There is increasing attention being paid to the synthesis and properties of $(Al_xGa_{1-x})_2O_3$.[1–14] The alloying of Ga_2O_3 with Al_2O_3 allows for tuning the bandgap over a very large range, particularly when the α-polytype is used, since this has a larger bandgap than the more commonly used and most stable β-polytype.[1,2,15–29] The larger bandgap means a wider range of absorption energies for photons, as well as a higher critical electric field in rectifiers and transistors.[30–35] The applications for these alloys, therefore, naturally range from high power electronic devices to solar-blind UV photodetectors.[36–58] For power electronics, the total switching losses in a power switch tradeoff of conduction losses ($\sim Ec^3$ in the limit of slow switching) and dynamic switching losses ($\sim E_c^2$ for high frequency switching) and the common figures-of-merit (FOM) depend on this critical field,[59] ie.

$$\text{Unipolar FOM } V_B^2/R_{on} = \varepsilon\mu_n E_C^3/4$$

$$\text{Lateral power FOM } V_B^2/R_{on} = q\mu_{ch} n_s E_C^2$$

The critical field in semiconductors has been found by Kaplar[59] to depend on the bandgap to the power 1.86, ie $E_C \propto E_G^{1.86}$. Thus, the larger the bandgap, the larger critical field and the higher the power levels can be switched by the device. Varley[4] has estimated the breakdown field to be ~16 MV.cm^{-1} for $(Al_{0.8}Ga_{0.2})_2O_3$. The optical bandgap for α-$(Al_xGa_{1-x})_2O_3$ was originally reported as E_g (x) = 5.25 + 3.31 x,[12,40] but this has evolved as data from a wider range of growth methods has been accumulated.[4,23] This semi-stable rhombohedral phase has the same lattice structure as α-Al_2O_3 substrates.[19,49,60] While the corundum crystal structure α-polytype is metastable, it can be readily grown by non-equilibrium techniques over a broad composition range.[6–44] A number of methods have been used to grow this polymorph, including mist Chemical Vapor Deposition,[12] Pulsed Laser Deposition,[40,41] Molecular Beam Epitaxy[42,43] and Metal Organic Chemical Vapor Deposition.[50,55,56] A major issue with any semiconductor alloy system are the miscibility limits and it has proven challenging to maintain phase stability at high Al contents in β-polytype alloys in some growth methods.[2,4,23] There has been much less work on the synthesis and properties of α-$(Al_xGa_{1-x})_2O_3$ alloys.[2–12] The current miscibility limits for the various polymorphs have been summarized recently by von Wenckstern et al..[61]

In addition, the Al-containing alloys are expected to be even more radiation-hard than Ga_2O_3, which itself is considerably more resistance to radiation damage than Si or GaAs.[62] One issue with the large bandgap range accessible through the α-$(Al_xGa_{1-x})_2O_3$ alloys is the limited choice of dielectrics that are possible which could give nested band alignments with acceptable conduction and valence band offsets.[63]

In this paper we report the measurement of band alignment for Al_2O_3 deposited by Atomic Layer Deposition (ALD) on α-$Al_xGa_{1-x})_2O_3$ system using alloys grown by Pulsed Laser Deposition (PLD) over a wide composition range from x = 0.26–0.74. The band alignments are type I for x < 0.5 but staggered for x > 0.5.

Experimental

The α-$(Al_xGa_{1-x})_2O_3$ alloys were grown by PLD on 2 inch diameter large a-plane (11.0) sapphire substrates using the continuous composition spread (CCS) PLD technique using a KrF excimer laser (Coherent LPX Pro 305, 248 nm, 2.6 J.cm^{-2}) on and a segmented ceramic target (Ga_2O_3/Al_2O_3) under an O_2 partial pressure.[2,61,64–66] The cation ratio was determined by energy dispersive X-ray spectroscopy (EDX) and the crystal structure by X-ray diffraction (XRD). The cation gradient ranged between x = 0.13 and x = 0.84 as measured by Energy Dispersive X-ray Spectroscopy (EDAX). The rhombohedral crystal structure of the thin films was confirmed by the 2θ-ω XRD scans. For x ~ 0.55, a change from relaxed to pseudomorphic growth was observed as confirmed by the evolution of in- and out-of-plane lattice constants. We examined four compositions, x = 0.26, 0.42, 0.58 and 0.74. More details on these samples can be found in Hassa et al..[22–24] The structural properties of the films were also examined by Transmission Electron Microscopy (TEM) and EDAX to measure interfacial stability and map the elemental composition near the interface. As the corundum structure is the thermodynamically most stable phase of Al_2O_3, the growth of ternary $(Al,Ga)_2O_3$ is feasible without miscibility gap, potentially enabling bandgap engineering between 5.0 and 8.8 eV.[22–24] Due to its optical transparency, high temperature and chemical stability, high mechanical strength and its

*Electrochemical Society Member.
**Electrochemical Society Fellow.
[z]E-mail: spear@mse.ufl.edu

low-cost industrial manufacturing capabilities, α-Al_2O_3 is the most common substrate for α-polymorph alloys.

The Al_2O_3 layers were deposited by Atomic Layer Deposition (ALD) at 200°C using the plasma mode in a Cambridge Nano Fiji 200.[63,64] The precursors were trimethylaluminum precursor and an inductively coupled plasma (ICP) of O_2 at 300 W.[47,48] After solvent cleaning, the substrates were exposed to Ozone for 15 min to form a protective oxide that is easily thermally desorbed during the ALD step. Both thick (200 nm) and thin (1.5 nm) layers of Al_2O_3 were deposited for measuring bandgaps and core levels on the α-$(Al_xGa_{1-x})_2O_3$ using the Kraut method.[67] A schematic of the samples used are shown in Fig. 1.[31]

In order to ensure the samples were appropriate for measuring the band alignments from the core levels, XPS survey scans were performed to measure the chemical state of the Al_2O_3 and $(Al_xGa_{1-x})_2O_3$ layers with an Al X-ray source (energy 1486.6 eV, source power 300W) [65,66]. Details of the measurement conditions have been described in detail previously.[63,64] The total energy resolution of the system is 0.5 eV, and the accuracy of the observed binding energy is $\sim$ 0.03 eV. Charge compensation was performed using an electron flood gun and simultaneous ion beam.[68–70] The samples were electrically insulated from the chuck to avoid uneven charge dispersion.[71] All electron analyzers and equipment were grounded. Differential charging was not observed with use of the electron gun.[47,48]

The Al_2O_3 bandgap was 6.9 eV, obtained from Reflection Electron Energy Loss Spectroscopy (REELS).[63] The bandgaps of the $(Al_xGa_{1-x})_2O_3$ at each composition were obtained from XPS energy loss measurements of the O1S peak.[63,64,70] The samples were also examined by cross-sectional Transmission Electron Microscopy (TEM) and EDAX to examine crystal quality and map the elemental composition near the interface. The electron transparent cross-sectional lamellae of $\sim$100 nm thick were prepared using FEI Helios Nanolab 660 dual beam focused ion beam. The bright field TEM images, selected area electron diffraction (SAED) patterns, and the EDAX mappings were obtained in FEI Talos F200X scanning/transmission electron microscope (S/TEM) equipped with an EDAX detector using field emission gun and 200 kV of acceleration voltage.

Results and Discussion

The cross-sectional TEM images of the 26% Al films are shown in Figs. 2a and 2b. The thickness of the film is found to be $\sim$250 nm with a clean film-substrate interface (shown in inset of Fig. 2b).The SAED pattern obtained on the film and substrate are shown in Figs. 2c and d, respectively. The substrate diffraction pattern exhibits hexagonal crystal structure, as expected from the α-Al_2O_3 substrate. The complex diffraction pattern of the α-$(Al_xGa_{1-x})_2O_3$ film incorporates additional spots relative to the substrate representing polycrystalline nature of the film. The calculated d-spacing values of the planes (1 1 2), (0 2 2), (0 2 3), and (0 −1 4) are found to be 2.65, 1.82, 1.41, and 0.94, respectively, confirming the planes of α-Ga_2O_3. Figure 2e represents the nano-diffraction pattern of the film on a single crystal along [1 0 0] zone axis of α-Ga_2O_3. Hassa[22] et al. have previously reported a detailed account of the structural and elastic properties of these films and found a transition from relaxed to pseudomorphic growth for Al contents >0.55. At lower Al compositions, the lattice constants follow Vegard's law. Knei β et al.[34] have recently reviewed the strain states and lattice relaxation for growth of similar films. The STEM HAADF image and corresponding EDAX maps taken in cross-section represent uniform distributions of the Al, Ga, and O in the films, as shown in Fig. 3.

Figures 4a and 4b show the cross-sectional TEM images of the 74% Al films. These films are $\sim$265 nm thick and are in the pseudomorphic regime of growth of α-$(Al_xGa_{1-x})_2O_3$ on sapphire. Similar to 26% Al film, the SAED patterns (Fig. 4c) of the 74% Al film contains randomly orientated polycrystalline of Ga_2O_3. The pronounced diffusive ring patterns of the 74% Al film demonstrate reduced grain size with the increase of Al content. The d-spacing values of the planes (0 −1 1), (0 0 2), (0 2 3), and (2 4 4) are found to be 2.49, 2.06, 1.43, and 1.15 Å, respectively, representing the planes of α-Ga_2O_3. The indexed nano-diffraction pattern obtained on a single crystal of α-Ga_2O_3 along [1 1 0] zone axis is shown in Fig. 4 €. The EDAX of 74% Al film also shows uniform incorporation of the lattice constituents, as shown in Fig. 5.

Figure 6 shows the high resolution XPS spectra for the α-$(Al_xGa_{1-x})_2O_3$ to Al_2O_3 vacuum-core delta regions of the four compositions, while the data for the Al_2O_3 is shown in Fig. 7. The valence band offsets were extracted from the shift of the core levels for the heterostructure samples with the thin dielectric on top of the four different compositions of the alloy. A compilation of the valence band maxima (VBM) are collected in Table I, with values of 2.7 ± 0.15 for x = 0.26, 3.3 ± 0.15 for x = 0.42, 4.4 ± 0.15 for x = 0.58 and 4.5 ± 0.15 for x = 0.74. These were obtained by fitting of the leading edge of the valence band. The error bars in the different binding energies were combined in a root sum square relationship to determine the overall error bars in the valence band offsets (ΔE_V).[64] These band offsets are then obtained by measuring the shift of the core levels in the α- $(Al_xGa_{1-x})_2O_3$ when Al_2O_2 was deposited. These are also tabulated in Table I, with values of −1.2 for x = 0.26, −0.2 for x = 0.42, 0.2 for x = 0.58 and 0.4 for x = 0.74.

Once the valence band offsets are established, to determine the conduction band offset, it is necessary to measure the band gap of each composition. We measured the bandgaps of the four $(Al_xGa_{1-x})_2O_3$ compositions from the separation between the core level peak energy and the onset of inelastic (plasmon) losses in each O 1s photoemission spectra.[63] To find the band-gap energy, a linear fit is made to the measured loss spectra curve near the approximate location of onset of inelastic losses. Next, by subtracting the background, the "zero" level is determined. The energy corresponding to the onset of inelastic losses is found by extrapolating

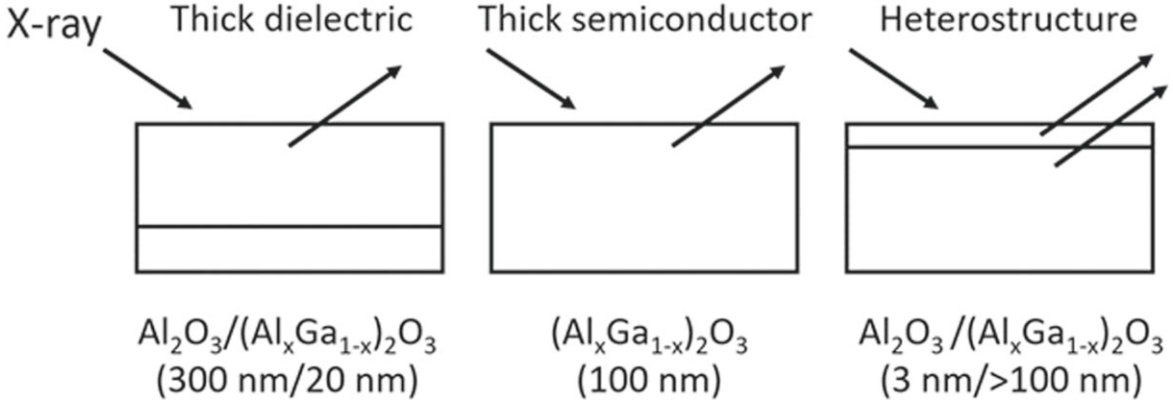

Figure 1. Schematic of the three types of samples measured to obtain the band alignments of Al_2O_3 on $(Al_xGa_{1-x})_2O_3$.

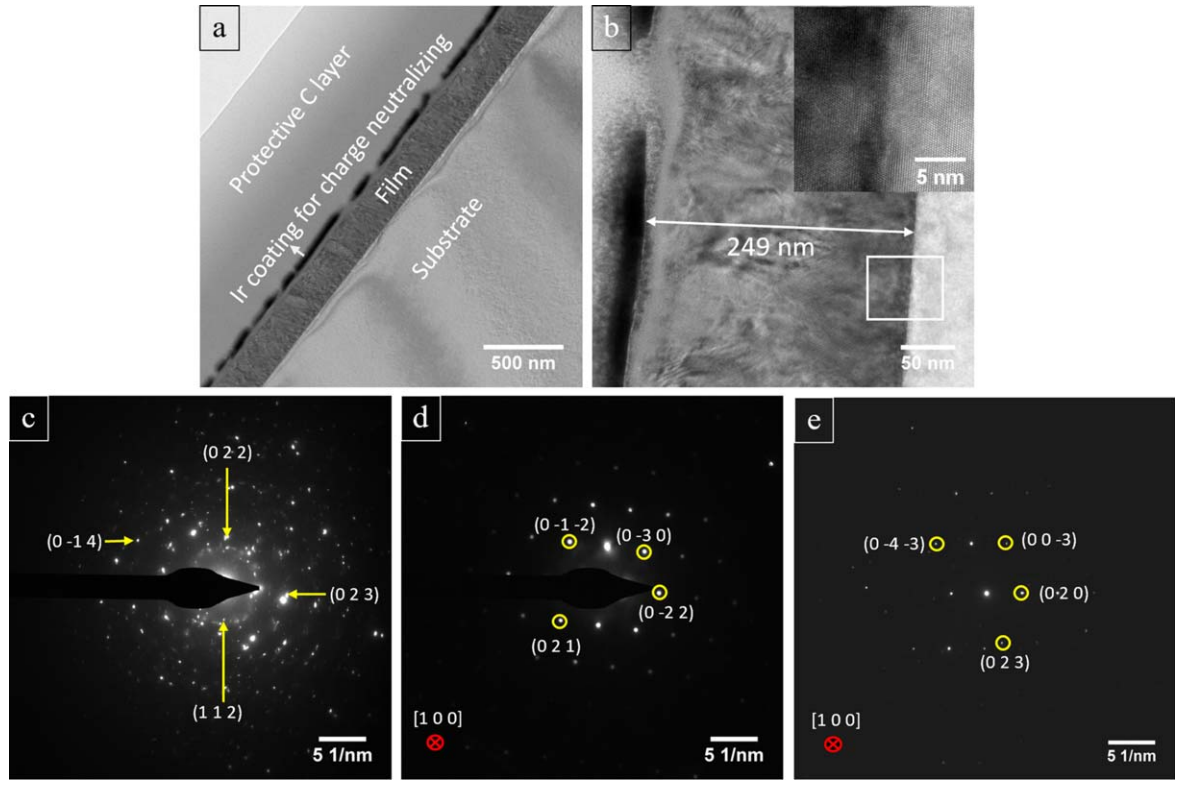

Figure 2. Bright field TEM images of the cross-section of 26% Al film (a)–(b). The HR-TEM image of film-substrate interface is shown in inset of (b). The SAED patterns of the (c) film and (d) substrate. (e) Nano-diffraction of the film along [1 0 0] zone axis.

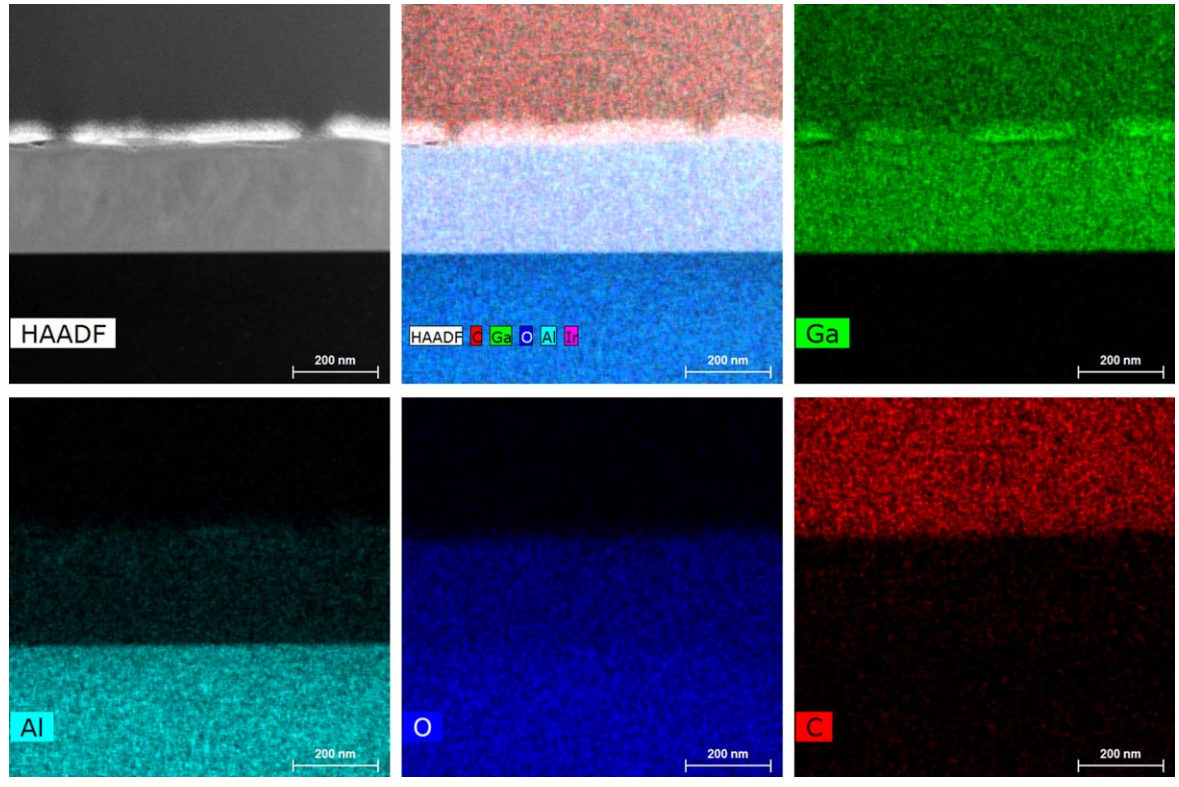

Figure 3. The STEM HAADF image and corresponding EDAX mapping of the 26% Al film.

the linear-fit line and determining its intersection with the zero level.[46] The bandgap energy is obtained from the the difference between the core-level peak energy and the onset of inelastic losses.[70]

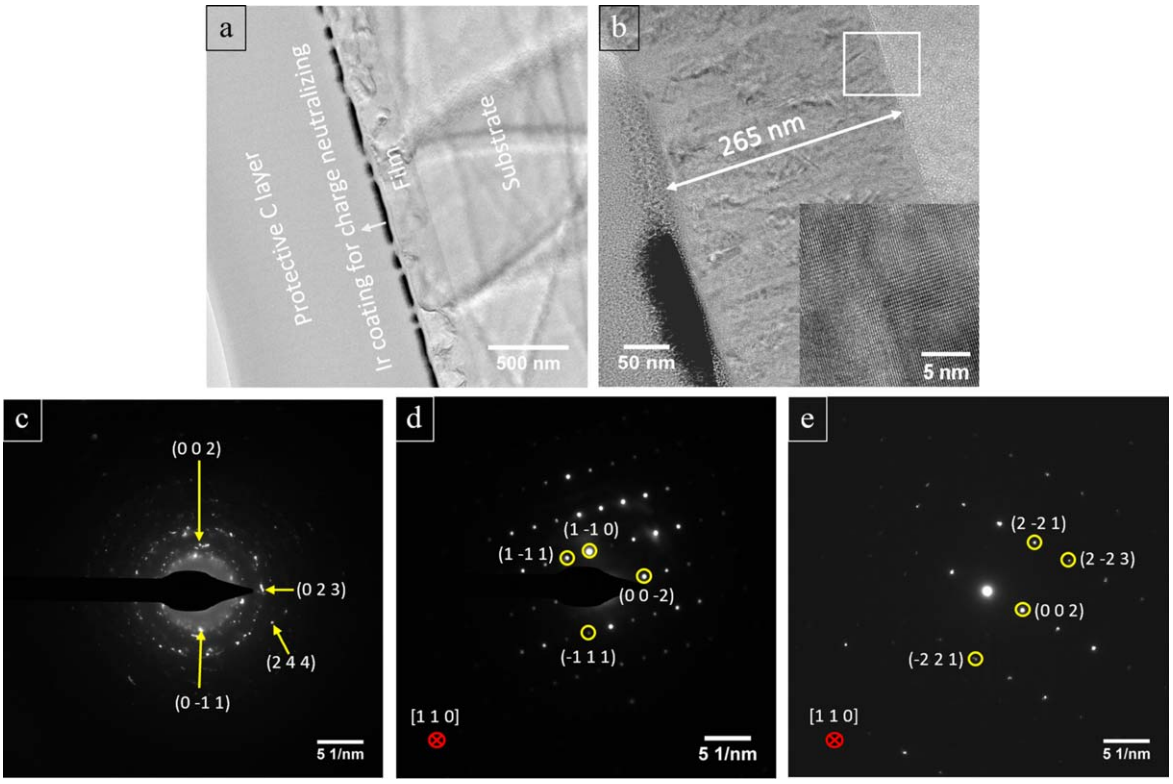

Figure 4. Bright field TEM images of the cross-section of 74% Al film (a)–(b). The HR-TEM image of film-substrate interface is shown in inset of (b). The SAED patterns of the (c) film and (d) substrate. (e) Nano-diffraction of the film along [1 1 0] zone axis.

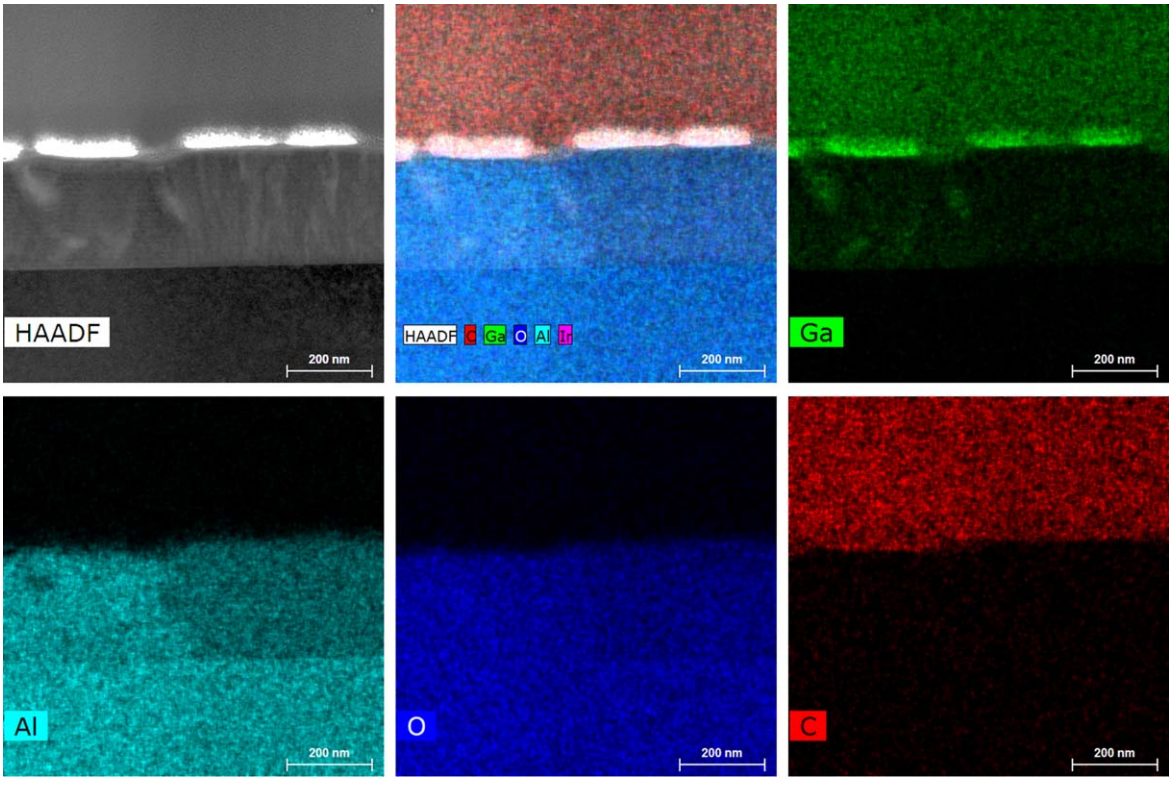

Figure 5. The STEM HAADF image and corresponding EDAX mapping of the 74% Al film.

The bandgap energies determined from the onset of photoemission inelastic losses in X-ray photoelectron spectroscopy were 5.8 eV for x = 0.26, 6.1 eV for x = 0.42, 6.4 eV for x = 0.58 and 7 eV for x = 0.74, respectively. The relationship between bandgap of the alloys and Al composition for our samples as a function of composition, x, is given by[4,31]

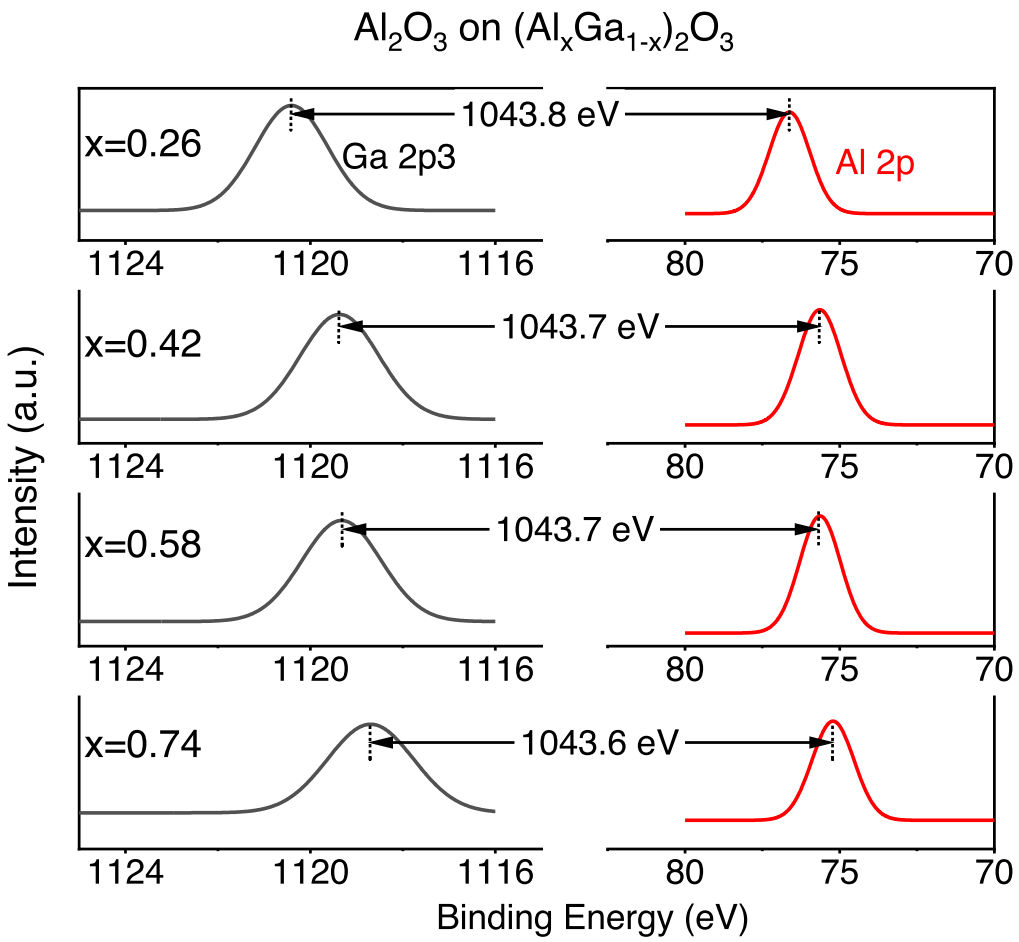

Figure 6. XPS spectra of core levels to valence band maximum (VBM) for reference $(Al_xGa_{1-x})_2O_3$ with x = 0.26, 0.42,0.58 or 0.74 (top to bottom) Aluminum, and (c) ALD thick film Al_2O_3 and Al_2O_3.The intensity is in arbitrary units (a.u.).

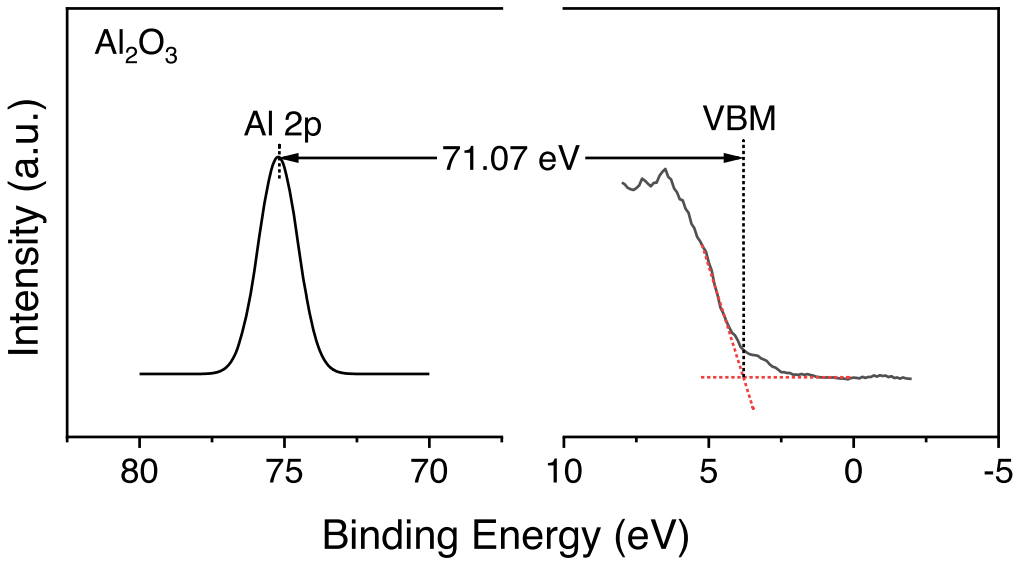

Figure 7. XPS spectra of core levels to valence band maximum (VBM) for ALD thick film Al_2O_3.The intensity is in arbitrary units (a.u.).

$$E_G(x) = (1-x)E_G^{GaO} + xE_G^{AlO} - bx\,(1-x)$$

where E_G^{GaO} and E_G^{AlO} are the bandgaps of the α-polytype binary endpoints and b is the bowing parameter. This has been previously reported in the range 1.1–1.6.[4,15,40] We get a value closer to 3 for our samples in the composition range measured. This is not unusual, given differences in strain due to growth temperature differences between the various growth methods and differences in buffer layers employed.

The conduction band offsets ΔE_C were obtained from the relation

Table I. XXX.

	Reference $(Al_xGa_{1-x})_2O_3$			Reference Al_2O_3			Thin Al_2O_3 on $(Al_xGa_{1-x})_2O_3$	
Aluminum Concentration	Core Level Peak (Ga $2p_{3/2}$)	VBM	Core - VBM	Core Level Peak (Al 2p)	VBM	Core - VBM	Δ Core Level (Ga $2p_{3/2}$- Al 2p)	Valence Band Offset
$(Al_{0.26}Ga_{0.74})_2O_3$	1117.7	2.7 ± 0.15	1115	74.32	3.25	71.07	1043.8	0.13
$(Al_{0.42}Ga_{0.58})_2O_3$	1118.2	3.3 ± 0.15	1114.9	—	—	—	1043.7	0.13
$(Al_{0.58}Ga_{0.42})_2O_3$	1119.2	4.5 ± 0.15	1114.7	—	—	—	1043.7	−0.07
$(Al_{0.74}Ga_{0.26})_2O_3$	1118.9	4.4 ± 0.15	1114.5	—	—	—	1043.6	−0.17

$$\Delta E_C = E_G^{Al_2O_3} - E_G^{AlGaO} - \Delta E_V$$

The corresponding conduction band offsets were 0.97 eV (x = 0.26), 0.67 eV (x = 0.46), 0.57 eV (x = 0.58) and 0.07 eV (x = 0.74).

Figure 8 shows the band diagrams for the $Al_2O_3/\alpha(Al_xGa_{1-x})_2O_3$ heterostructure. The Al_2O_3 has adequate conduction band offsets, but the valence band offsets are small and actually negative at x < 0.5. There would be inadequate confinement of holes in Al_2O_3/α-$(Al_xGa_{1-x})_2O_3$ samples over the entire composition range. The conduction band offsets are high enough to provide effective electron confinement. The $Al_2O_3/(Al_xGa_{1-x})_2O_3$ band alignment is type I for x > 0.5 and staggered for x < 0.5. We have recently found that SiO_2 deposited on the α- $(Al_xGa_{1-x})_2O_3$ alloys shows band alignments that are staggered type II for x < 0.5 and straddling type I for x > 0.5, with conduction band offsets >1.3 eV across the composition range examined.[72] Even this large gap dielectric will only provide adequate valence band offsets over a limited range of compositions.[72] Note also that we find the bandgap of the ALD Al_2O_3 is slightly smaller than the $\alpha(Al_{0.74}Ga_{0.26})_2O_3$, which is a common feature when comparing amorphous thin films to polycrystalline films.[22–26] The optical bandgap of a-Al_2O_3 single crystal is 8.7–8.8 eV.

Summary and Conclusions

The valence band offsets of $Al_2O_3/\alpha(Al_xGa_{1-x})_2O_3$ heterojunctions were measured over a range of Al contents (x = 0.26 − 0.74). The band alignments are nested type-I for x < 0.5 and staggered type-II for x > 0.5, with conduction band offsets of 0.97 eV at low Al composition but only 0.07 eV for x = 0.74 eV. Tis illustrates the difficulty in finding appropriate dielectrics for an alloy system whose bandgaps span such a large range. The thermal stability of this system is of interest for future work, as the α-polytype I not the most energetically favorable state, although kinetically limited processes such as rapid thermal annealing will be able to be used in device processing steps without major issues. The alpha AlGaO/GaO heterojunction band offsets need more work to find dielectrics with adequate conduction and valence band offsets since these heterojunctions are seriously considered for use in alpha AlGaO/GaO MODFETs. The c-lattice constant follows the relaxed grown part Vegard's law and aligned in the pseudomorphic part at around 12.99 Å, which corresponds to the value of α-Al_2O_3. Since the α-phase can be stabilized across the entire composition range of the $(Al,Ga)_2O_3$ alloy, this structure is particularly suited for the realization of high performance power devices. Further investigations should also be carried out on the α-phase focused on a more in-depth analysis of the relaxed or pseudomorphic growth as a function of layer thickness or the substrate used.[22–24]

Acknowledgments

The work was performed as part of Interaction of Ionizing Radiation with Matter University Research Alliance (IIRM-URA), sponsored by the Department of the Defense, Defense Threat Reduction Agency under award HDTRA1-20-2-0002. The content of the information does not necessarily reflect the position or the policy of the federal government, and no official endorsement should be inferred. The work at PSU was partially supported by the NSF ECCS 2015795. The work at UF was also supported by NSF DMR 1856662 (James Edgar). The work at Leipzig was supported by the European Social Fund within the Young Investigator Group "Oxide Heterostructures" (SAB 100310460), by Universität Leipzig in research profile area "Complex Matter" as well as within the framework of GraFOx, a Leibniz-Science Campus partially funded by the Leibniz Association. The authors at Leipzig thank Jörg Lenzner for EDX measurements and Monika Hahn for PLD target preparation.

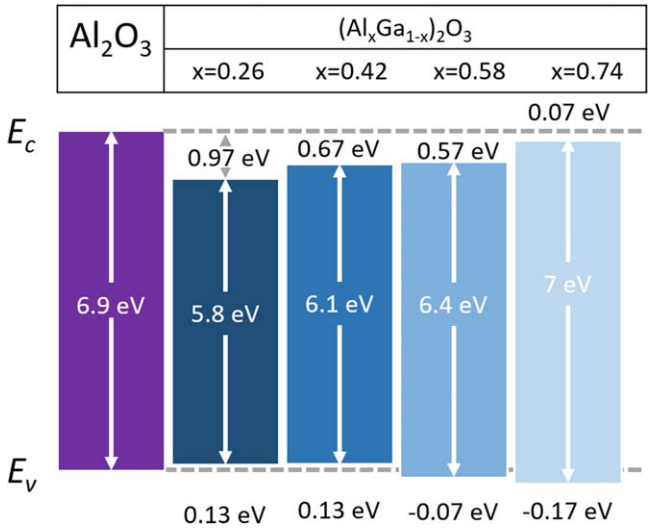

Figure 8. Band diagrams for the Al_2O_3/α-$(Al_xGa_{1-x})_2O_3$ heterostructure in which the Al_2O_3 was deposited by ALD.

ORCID

S. J. Pearton https://orcid.org/0000-0001-6498-1256

References

1. E. Ahmadi and Y. Oshima, *J. Appl. Phys.*, **126**, 160901 (2019).
2. H. von Wenckstern, *Advanced Electronic Mater*, **3**, 1600350 (2017).
3. B. Krueger, C. Dandeneau, E. M. Nelson, S. T. Dunham, F. S. Ohuchi, and M. A. Olmstead, *J. Am. Ceram. Soc.*, **99**, 2467 (2016).
4. J. B. Varley, *J. Mater. Res.*, **36**, 4790 (2021).
5. R. Wakabayashi, K. Yoshimatsu, M. Hattori, J.-S. Lee, O. Sakata, and A. Ohtomo, *Cryst. Growth Des.*, **21**, 2844 (2021).
6. Y. Oshima, E. G. Víllora, and K. Shimamura, *Appl. Phys. Express*, **8**, 055501 (2015).
7. D. Machon, P. F. McMillan, B. Xu, and J. Dong, *Phys. Rev.*, **73**, 094125 (2006).
8. D. Shinohara and S. Fujita, *Jpn. J. Appl. Phys.*, **47**, 7311 (2008).
9. H. Kim, H. Ko, Y.-C. Chung, and S. B. Cho, *J. Eur. Ceram. Soc.*, **41**, 611 (2020).
10. A. Hassa, C. Sturm, M. Kneiß, D. Splith, H. von Wenckstern, T. Schultz, N. Koch, M. Lorenz, and M. Grundmann, *APL Mater.*, **8**, 021103 (2020).
11. R. Jinno, T. Uchida, K. Kaneko, and S. Fujita, *Appl. Phys. Express*, **9**, 071101 (2016).
12. S. Fujita and K. Kaneko, *J. Cryst. Growth*, **401**, 588 (2014).
13. K. Kaneko, K. Suzuki, Y. Ito, and S. Fujita, *J. Cryst. Growth*, **436**, 150 (2016).
14. R. Jinno, K. Kaneko, and S. Fujita, *Japan J Appl Phys*, **60** (2021), SB SBBD13.
15. R. Jinno et al., *Sci. Adv.*, **7**, eabd5891 (2021).
16. H. Takane, K. Kaneko, Y. Ota, and S. Fujita, *J. J. Appl. Phys*, **60**, 055501 (2021).
17. Z. Chen, M. Arita, K. Saito, T. Tanaka, and Q. Guo, *AIP Adv.*, **11**, 035319 (2021).
18. S. Mu, M. Wang, H. Peelaers, and C. G. Van de Walle, *APL Mater.*, **8**, 091105 (2020).
19. M. Hilfiker, U. Kilic, A. Mock, V. Darakchieva, S. Knight, R. Korlacki, A. Mauze, Y. Zhang, J. Speck, and M. Schubert, *Appl. Phys. Lett.*, **114**, 231901 (2019).
20. M. Oda, R. Tokuda, H. Kambara, T. Tanikawa, T. Sasaki, and T. Hitora, *Appl. Phys. Express*, **9**, 021101 (2016).
21. K. Akaiwa, K. Kaneko, K. Ichino, and S. Fujita, *Jpn. J. Appl. Phys.*, **55**, 1202BA (2016).
22. A. Hassa, P. Storm, M. Kneiß, D. Splith, H. von Wenckstern, M. Lorenz, and M. Grundmann, *Phys. Status Solidi B*, **258**, 2000394 (2021).
23. A. Hassa, M. Grundmann, and H. von Wenckstern, *J. Phys. D: Appl. Phys.*, **54**, 223001 (2021).
24. A. Hassa, C. Wouters, M. Kneiß, D. Splith, C. Sturm, H. von Wenckstern, M. Albrecht, M. Lorenz, and M. Grundmann, *J. Phys. D: Appl. Phys.*, **53**, 485105 (2020).
25. J. E. N. Swallow, R. G. Palgrave, P. A. E. Murgatroyd, A. Regoutz, M. Lorenz, A. Hassa, M. Grundmann, H. von Wenckstern, J. B. Varley, and T. D. Veal, *ACS Appl. Mater. Interfaces* (2021).
26. Y. Oshima, K. Kawara, T. Shinohe, T. Hitora, M. Kasu, and S. Fujita, *APL Mater.*, **7**, 022503 (2019).
27. Y. Oshima, *Heteroepitaxial Growth of α and ε-Ga_2O_3* (Gallium Oxide)(Crystal Growth, Materials Properties, and Devices) (2019), Springer.
28. H. Sun, K.-H. Li, C. G. T. Castanedo, S. Okur, G. S. Tompa, T. Salagaj, S. Lopatin, A. Genovese, and X. Li, *Cryst. Growth Des.*, **18**, 2370 (2018).
29. Y. W. Zhang et al., *Appl. Phys. Lett.*, **112**, 173502 (2018).
30. F. B. Zhang, K. Saito, T. Tanaka, M. Nishio, M. Arita, and Q. X. Guo, *Appl. Phys. Lett.*, **105**, 162107 (2014).

31. T. Uchida, R. Jinno, S. Takemoto, K. Kaneko, and S. Fujita, *Jpn. J. Appl. Phys.*, **57**, 040314 (2018).
32. Q. Feng, X. Li, G. Han, L. Huang, F. Li, W. Tang, J. Zhang, and Y. Hao, *Opt. Mater. Express*, **7**, 1240 (2017).
33. V. Gottschalch, S. Merker, S. Blaurock, M. Kneiß, U. Teschner, M. Grundmann, and H. Krautscheid, *J. Cryst. Growth*, **510**, 76 (2019).
34. M. Kneiß, D. Splith, H. von Wenckstern, M. Lorenz, T. Schultz, N. Koch, and M. Grundmann, *J. Mater. Res.*, **36**, 4816 (2021).
35. C. Kranert, M. Jenderka, J. Lenzner, M. Lorenz, H. von Wenckstern, R. Schmidt-Grund, and M. Grundmann, *J. Appl. Phys.*, **117**, 125703 (2015).
36. B. Mazumder, J. Sarker, Y. Zhang, J. M. Johnson, M. Zhu, S. Rajan, and J. Hwang, *Appl. Phys. Lett.*, **115**, 132105 (2019).
37. B. Mazumder and J. Sarker, *J. Mater. Res.*, **36**, 52 (2020).
38. S.-H. Yuan, C.-C. Wang, S.-Y. Huang, and D.-S. Wuu, *IEEE Electron Dev. Lett.*, **39**, 220 (2018).
39. H. Peelaers, J. B. Varley, J. S. Speck, and C. G. Van de Walle, *Appl. Phys. Lett.*, **112**, 242101 (2018).
40. G. T. Dang, T. Yasuoka, Y. Tagashira, T. Tadokoro, W. Theiss, and T. Kawaharamura, *Appl. Phys. Lett.*, **113**, 062102 (2018).
41. M. Grundmann and M. Lorenz, *APL Mater.*, **8**, 021108 (2020).
42. R. Kumaran, T. Tiedje, S. E. Webster, S. Penson, and W. Li, *Optics Lett*, **35**, 3793 (2010).
43. E. Ahmadi, O. S. Koksaldi, X. Zheng, T. Mates, Y. Oshima, U. K. Mishra, and J. S. Speck, *Appl. Phys. Express*, **10**, 071101 (2017).
44. F. Zhang, K. Saito, T. Tanaka, M. Nishio, M. Arita, and Q. Guo, *Appl. Phys. Lett.*, **105**, 162107 (2014).
45. H. Ito, K. Kaneko, and S. Fujita, *Jpn. J. Appl. Phys.*, **51**, 100207 (2012).
46. S. Krishnamoorthy et al., *Appl. Phys. Lett.*, **111**, 023502 (2017).
47. Y. Zhang, C. Joishi, Z. Xia, M. Brenner, S. Lodha, and S. Rajan, *Appl. Phys. Lett.*, **112**, 233503 (2018).
48. J. B. Varley, A. Perron, V. Lordi, D. Wickramaratne, and J. L. Lyons, *Appl. Phys. Lett.*, **116**, 172104 (2020).
49. T. Wang, W. Li, C. Ni, and A. Janotti, *Phys. Rev. Appl.*, **10**, 011003 (2018).
50. A. F. M. Anhar Uddin Bhuiyan, Z. Feng, J. M. Johnson, Z. Chen, H. L. Huang, J. Hwang, and H. Zhao, *Appl. Phys. Lett.*, **115**, 120602 (2019).
51. R. Wakabayashi, T. Oshima, M. Hattori, K. Sasaki, T. Masui, A. Kuramata, S. Yamakoshi, K. Yoshimatsu, and A. Ohtomo, *J. Cryst. Growth*, **424**, 77 (2015).
52. S. W. Kaun, F. Wu, and J. S. Speck, *J. Vac. Sci. Technol.*, **33**, 041508 (2015).
53. R. Miller, F. Alema, and A. Osinsky, *IEEE Trans. Semicond. Manuf.*, **31**, 467 (2018).
54. J. P. McCandless et al., *Appl. Phys. Lett.*, **119**, 062102 (2021).
55. A. F. M. A. U. Bhuiyan, Z. Feng, J. M. Johnson, H. L. Huang, J. Sarker, M. Zhu, M. R. Karim, B. Mazumder, J. Hwang, and H. Zhao, *APL Mater.*, **8**, 031104 (2020).
56. A. F. M. A. U. Bhuiyan, Z. Feng, J. M. Johnson, H.-L. Huang, J. Hwang, and H. Zhao, *Cryst. Growth Des.*, **20**, 6722 (2020).
57. J. M. Johnson et al., *APL Mater.*, **9**, 051103 (2021).
58. J. Sarker, S. Broderick, A. F. M. A. U. Bhuiyan, Z. Feng, H. Zhao, and B. Mazumder, *Appl. Phys. Lett.*, **116**, 152101 (2020).
59. R. J. Kaplar, *'Analysis of the Dependence of Critical Electric Field on Semiconductor Bandgap* (ECS Meeting, Atlanta, GA) (2019), (https://osti.gov/servlets/purl/1642836).
60. A. Ratnaparkhe and W. R. L. Lambrecht, *Phys. Status Solidi*, **257**, 1900317 (2020).
61. H. von Wenckstern, D. Splith, and M. Grundmann, *Pulsed Laser Deposition-2, in Gallium Oxide: Materials Properties, Crystal Growth, and Devices*, ed. M. Higashiwaki and S. Fujita (Springer International Publishing, Cham) (2020) p. 273.
62. C. Fares, Z. Islam, A. Haque, M. Kneiß, H. von Wenckstern, M. Grundmann, M. Tadjer, F. Ren, and S. J. Pearton, *ECS J. Sol State Sci. Technol.*, **8**, P751 (2019).
63. C. Fares, M. Kneiß, H. von Wenckstern, M. Tadjer, F. Ren, E. Lambers, M. Grundmann, and S. J. Pearton, *ECS J. Sol State Sci. Technol.*, **8**Q, P351 (2019).
64. H. von Wenckstern, M. Kneiß, A. Hassa, P. Storm, D. Splith, and M. Grundmann, *Phys. Status Solidi*, **257**, 1900626 (2020).
65. H. von Wenckstern, M. Kneiß, A. Hassa, P. Storm, D. Splith, and M. Grundmann, *Phys. Status Solidi*, **49**, 213001 (2019).
66. H. von Wenckstern, Z. Zhang, F. Schmidt, J. Lenzner, H. Hochmuth, and M. Grundmann, *Cryst. Eng. Comm*, **15**, 10020 (2013).
67. E. A. Kraut, R. W. Grant, J. R. Waldrop, and S. P. Kowalczyk, *Phys. Rev. Lett.*, **44**, 1620 (1980).
68. A. G. Shard, *J. Vac. Sci. Technol.*, **38**, 041201 (2020).
69. C. J. Powell, *Microsc. Today*, **24**, 16 (2016).
70. L. Wang, Y. Du, and S. A. Chambers, *J. Vac. Sci. Technol.*, **A39**, 043208 (2021).
71. D. R. Baer, K. Artyushkova, H. Cohen, C. D. Easton, M. Engelhard, T. R. Gengenbach, G. Greczynski, P. Mack, D. J. Morgan, and A. Roberts, *J. Vac. Sci. Technol.*, **38**, 031204 (2020).
72. X. Xia, C. Fares, F. Ren, A. Hassa, H. von Wenckstern, M. Grundmann, and S. J. Pearton, *ECS J. Solid State Sci. Technol.*, **10**, 113007 (2021).